

1 **The Production of Small Primary Craters on Mars and the Moon**

2

3 J.-P. Williams*, A. V. Pathare, O. Aharonson

4

5 Jean-Pierre Williams*

6 Dept. Earth and Space Sciences

7 University of California

8 Los Angeles, CA 90095, USA

9 jpierre@mars.ucla.edu

10 310-825-4414 (office)

11 310-825-2279 (fax)

12

13 Asmin V. Pathare

14 Planetary Science Institute

15 Tucson, AZ 85719, USA

16 pathare@psi.edu

17

18 Oded Aharonson

19 Center for Planetary Science

20 Weizmann Inst. Of Science

21 Rehovot, 76100 Israel

22 oa@caltech.edu

23

24

25

26

27

28

29

30

31

32

33 *Corresponding Author

34

35

36 Keywords: Cratering; Mars; Mars surface

37

38

39 **Abstract**

40 We model the primary crater production of small ($D < 100$ m) primary craters on Mars and the
41 Moon using the observed annual flux of terrestrial fireballs. From the size-frequency distribution
42 (SFD) of meteor diameters, with appropriate velocity distributions for Mars and the Moon, we
43 are able to reproduce martian and lunar crater-count chronometry systems (isochrons) in both
44 slope and magnitude. We include an atmospheric model for Mars that accounts for the
45 deceleration, ablation, and fragmentation of meteors. We find that the details of the atmosphere
46 or the fragmentation of the meteors do not strongly influence our results. The downturn in the
47 crater SFD from atmospheric filtering is predicted to occur at $D \sim 10$ -20 cm, well below the
48 downturn observed in the distribution of fresh craters detected by the Mars Global Surveyor
49 (MGS) Mars Orbiter Camera (MOC) or the Mars Reconnaissance Orbiter (MRO) Context
50 Camera (CTX). Crater counts conducted on the ejecta blanket of Zunil crater on Mars and North
51 Ray crater on the Moon yielded crater SFDs with similar slopes and ages (~ 1 Ma, and ~ 58 Ma,
52 respectively) to our model, indicating that the average cratering rate has been constant on these
53 bodies over these time periods. Since our Monte Carlo simulations demonstrate that the existing
54 crater chronology systems can be applied to date young surfaces using small craters on the Moon
55 and Mars, we conclude that the signal from secondary craters in the isochrons must be relatively
56 small, as our Monte Carlo model only generates primary craters.

57

58

59

60

61

62 **1. Introduction**

63 The accumulation of craters on a planetary surface can be used to determine relative ages
64 of areas of geologic interest. Assigning absolute ages is done with modeled impact crater
65 isochrons, a technique that has been developed over several decades (e.g. Hartmann, 1966;
66 Neukum and Wise, 1976; Hartmann, 1999; Neukum and Ivanov, 1994; Hartmann and Neukum,
67 2001; Hartmann, 2005). For crater ages on Mars, isochrons are derived from the size-frequency
68 distribution (SFD) of craters observed on the lunar maria for which we have dated Apollo
69 samples (Wilhelms, 1987), scaled to account for the ratio of meteoroids at the top the martian
70 atmosphere relative to the Moon's and the differences in gravity and average impact velocity of
71 intersecting orbits. The resulting isochrons yield an expected crater SFD for a given age surface
72 and provide a means of understanding the absolute timescale of major geological and
73 geophysical processes.

74 The SFD is typically described as a power-law with slope n . Deviations from the power-
75 law occur through various processes which, in general, preferentially alter the smaller diameter
76 crater population, making small craters more challenging to use for age-dating surfaces. Because
77 of the frequency at which small craters form however, they provide the ability to discriminate
78 surface ages of geologically young regions and features at a higher spatial resolution where only
79 small craters are available for dating. This level of resolution is required to establish the temporal
80 relation of recent geologic activity on Mars such as gully and landslide formation, volcanic
81 resurfacing, sedimentation, exhumation, dune activity, glaciation and other periglacial landforms,
82 and the possible relation of such features to obliquity cycles of $\sim 10^7$ y timescale (e.g. Basilevsky
83 et al., 2009; Burr et al., 2002; Hartmann and Berman, 2000; Kadish et al., 2008; Lanagan et al.,

84 2001; Malin and Edgett, 2000a, 2000b, 2001; Mangold, 2003; Marquez et al., 2004; Quantin et
85 al., 2007; Reiss et al., 2004; Shean et al., 2006; Schon et al., 2009).

86 The Mars Obiter Camera (MOC) aboard the Mars Global Surveyor (MGS), with ~ 1.5 m
87 resolution/pixel (Malin et al., 1992), identified 19 fresh craters over a ~ 6.8 year period (Malin et
88 al., 2006). Data from the High Resolution Imaging Science Experiment (HiRISE) aboard the
89 Mars Reconnaissance Orbiter (MRO) is currently providing image data with up to 25 cm pix^{-1}
90 resolution (McEwen et al., 2007a), and has imaged and confirmed >200 small (< 50 m diameter)
91 fresh impact craters having formed within the last few decades following their discovery by the
92 Context (CTX) camera (Malin et al., 2007) on the same spacecraft (Byrne et al., 2009; Daubar et
93 al., 2010, 2011, 2012; Daubar and McEwen, 2009; Dundas and Byrne, 2010; Ivanov et al., 2008,
94 2009, 2010; Kennedy and Malin, 2009; McEwen et al., 2007b, 2007c). This offers an
95 opportunity to study the production of small meter-scale craters on the surface of Mars in greater
96 detail and refine isochron models for dating young surfaces on Mars.

97 In this paper, we model crater populations using a Monte Carlo simulation to explore the
98 primary crater production function at small diameters and the potential influence of present-day
99 atmospheric filtering. We explore ablation, deceleration, and fragmentation of projectiles as they
100 traverse the martian atmosphere and compare our results with the 44 fresh craters reported by
101 Daubar et al. (2013) that have been well constrained by CTX before- and after-images. We then
102 assess the current impact-crater isochron model of Hartmann (2005) and the estimated ratio of
103 meteoroids at the top of the martian atmosphere relative to the top of the terrestrial atmosphere,
104 which is the primary source of uncertainty in isochron models (Hartmann, 2005).

105

106 **2. Model**

107 2.1 Meteoroids traversing the atmosphere

108 Crater populations are modeled assuming a power law distribution of projectiles at the top of the
109 atmosphere and account for possible fragmentation and the dependence of mass and velocity on
110 deceleration and ablation in the atmosphere. The size distribution of projectiles at the top of
111 Mars' atmosphere is adapted from the power-law fit to satellite observations of the annual flux of
112 near-Earth objects colliding with the Earth for objects with diameters < 200 m (Brown et al.,
113 2002): $\log(N) = c_0 - d_0 \log(D_p)$, where N is the cumulative number of bolides colliding with the
114 Earth per year, D_p is the meteoroid diameter in meters, $c_0 = 1.568$, and $d_0 = 2.70$. This SFD has
115 been scaled by a factor 2.6, the nominal ratio of meteoroids at the top of Mars' atmosphere
116 relative to the Moon from the latest isochron model iteration of Hartmann (2005),

117 The kinetic energy of an object entering the atmosphere is lost to deceleration and
118 ablation. The decelerating force due to aerodynamic drag is (e.g., Baldwin and Sheaffer, 1971;
119 Chyba et al., 1993; Melosh, 1989)

$$\frac{dv}{dt} = \frac{C_D \rho_a A v^2}{2m} + g(z) \sin \theta \quad (1)$$

120 where ρ_a is the local density of the atmosphere. The parameters A , v , and m , are the cross-
121 sectional area, the velocity, and the mass of the object respectively, g is the local gravitational
122 acceleration at altitude z , and θ is the angle of the trajectory measured from the local horizontal

$$\frac{d\theta}{dt} = \frac{g(z) \cos \theta}{v} \quad (2)$$

123 Eq. 2 assumes a flat surface geometry and precludes the possibility of projectiles skipping out of
124 the atmosphere. The drag coefficient, C_D , is ~ 1 in the continuum flow regime (Podolak et al.,
125 1988). Heating of the projectile's surface during entry is efficiently shed by ablation

$$\frac{dm}{dt} = \frac{C_H \rho_a A v^3}{2\zeta} \quad (3)$$

126 where C_H is the heat transfer coefficient and ζ is the heat of ablation (Bronshten, 1983).

127 To assess the conditions in which deceleration and ablation become substantial, we
 128 employ a heuristic model. Taking the gravity term to be negligible in Eq. (1) for the moment, and
 129 the approximation of an exponential density scale height for the atmosphere, $\rho_a = \rho_o \exp(-z/H)$,
 130 where z is the altitude, H is the scale height, and ρ_o is the atmospheric density at the surface, the
 131 final mass of the meteor, m_f , can be related to the initial velocity, v_i , and final velocity, v_f , by

$$m_f = m_i \exp[-\sigma(v_i^2 - v_f^2)] \quad (4)$$

132 where m_i is the initial mass of the object at entry and $\sigma = C_H/(2\zeta C_D)$ is the ablation coefficient.

133 Combining the above equations and solving (e.g., Davis, 1993), the dependence of mass
 134 and velocity on deceleration and ablation can be seen (Figure 1). Smaller, faster objects are more
 135 readily filtered out by the atmosphere. The condition for significant deceleration can be
 136 estimated to occur when the meteoroid mass is equivalent to the column of atmospheric mass it
 137 encounters, $m_i \sim \rho_o H A$. Similarly, we can estimate the condition for substantial ablation. Ablation
 138 is more efficient at higher velocities as the ablative energy is proportional to the product of the
 139 drag force and the traversed distance, or, $dm \cdot \sigma^{-1} \propto \rho_a v^2 A \cdot v dt$. A transition to a high ablation
 140 regime will occur when the energy to ablate the entire meteoroid mass, $m \cdot \sigma^{-1}$, is equivalent to the
 141 energy required to traverse the atmosphere to the surface at a given velocity, $\rho_o H A \cdot v^2$, neglecting
 142 deceleration.

143 Using these criteria, we can classify the projectiles based on velocity and mass (Figure 2).
 144 For large, slow projectiles, $m_f \sim m_i$ and $v_f \sim v_i$, and the projectile will reach the surface relatively
 145 unchanged. For smaller, slow objects where $m < \rho_o H A$, and $dm/dt \sim 0$, the final velocity decreases

146 exponentially $v_f \sim v_i \exp \left[-\frac{\rho_o HA}{m \sin \theta} \right]$. Fast meteors, defined as having high initial velocities where
 147 $v_i^2 > \sigma^{-1}$, will experience significant ablation, $m_f < e^{-1} \cdot m_i$. Large, fast meteors will survive
 148 complete ablation if $m\sigma^{-1} < \rho_o HA \cdot v^2$, where the ablation will be limited by deceleration. These
 149 intermediate projectiles define the wedge shaped region in Figure 2a. Our taxonomic boundaries
 150 based on initial projectile masses and velocities are derived from our numeric modeling for a
 151 range of projectile masses and entry velocities (Figure 2).

152 **2.2 Monte Carlo simulation**

153 We generated model crater populations using a Monte Carlo simulation employing the power-
 154 law distribution of meteoroids entering the top of the atmosphere from the previous section and
 155 the normalized distribution of entry velocities at Mars (Bland and Smith, 2000; Davis, 1993;
 156 Flynn and McKay, 1990; Popova et al., 2003):

$$F(v_i) = 0.0231 v_i \exp \left[-\left(\frac{v_i - 1.806}{8.874} \right)^2 \right] \quad (4)$$

157 where $v_i \geq 5 \text{ km s}^{-1}$ (the escape velocity of Mars) with a mean velocity of 10.2 km s^{-1} . Following
 158 Love and Brownlee (1991), the probability distribution of entry angles is taken to be $\sin(2\theta)$,
 159 which has a maximum at 45° and drops to zero at 0° and 90° . A distribution of 5 groups of
 160 material types derived from the relative observed number of objects entering the terrestrial
 161 atmosphere is taken from Ceplecha et al. (1998). The material groups differ in their ability to
 162 penetrate the atmosphere, with the average ablation coefficient, σ , and bulk density, ρ_m , for each
 163 group listed in Table 1. Model results for ordinary chondrites are shown in Figure 3 for a single
 164 initial entry angle of 45° , demonstrating a good match with the results shown in Figure 1.

165 The resulting crater volumes from the projectiles impacting the surface can be described
 166 by a scaling law that relates impact velocity and projectile and target characteristics (see Melosh

167 (1989) for a review). In converting the crater SFD derived from the lunar surface to Mars,
 168 Hartmann (2005) assumes crater diameters, D , scale with impact energy as $E^{0.43}$ and with gravity
 169 as $g^{-0.17}$ to account for differences in mean impact velocity and gravitational acceleration
 170 between the two bodies. For small projectiles, the depth of excavation by an impact is small
 171 enough that lithostatic stresses are small relative to the characteristic yield stress of the regolith.
 172 In such cases the resulting transient crater diameter is determined by the yield strength, \bar{Y} , of the
 173 target material (“strength scaling”), and no longer scales with gravity. The transition from
 174 strength scaling to gravity scaling occurs when $\bar{Y} \sim \rho_t g R_p$ where R_p , the projectile radius, is taken
 175 to be the characteristic depth and ρ_t is the target density (Holsapple, 1993). For a regolith of
 176 density 2000 kg m^{-3} and yield strength of $0.1 - 1 \text{ MPa}$, the transition between strength and
 177 gravity dominated regimes occurs at $D \sim 27 - 270 \text{ m}$. This implies that the $1 - 10 \text{ m}$ scale fresh
 178 craters discovered by spacecraft over the last decade (Malin et al, 2006; Daubar et al., 2013) are
 179 predominately in the strength scaling regime. Strength scaling results in a reduction in crater
 180 volume relative to gravity scaled craters. As a consequence, the distribution of crater diameters
 181 would be expected to be shallower than that predicted by the isochrons of Hartmann (2005) at
 182 the smallest sizes, which assume all crater diameters scale with gravity.

183 The cratering efficiency, $\pi_v = \rho_t V / m_f$, where ρ_t is the target density and V is the transient
 184 crater volume, is proportional to (Holsapple, 1993):

$$\left(\pi_2 + \pi_3 \frac{2+\mu}{2} \right)^{-\frac{3\mu}{2+\mu}} \quad (4)$$

185 assuming impactor and target densities are the same, where μ is an empirical constant (ranging
 186 from $1/3 - 2/3$). The parameters π_2 and π_3 are dimensionless numbers describing the cratering
 187 efficiency for gravity scaling and strength scaling, respectively, where $\pi_2 = g R_p / v_f^2$, the ratio of
 188 the lithostatic pressure at a depth equivalent to the projectile radius and the initial dynamic

189 pressure generated by the impact, and $\pi_3 = \bar{Y}/\rho_t v_f^2$, the ratio of effective target yield strength to
 190 the initial dynamic pressure (Holsapple, 1993). For smaller projectiles, the π_2 term becomes
 191 negligible and π_3 becomes constant with impactor size, depending only on velocity and the
 192 material strength of the target. At large impactor sizes, π_2 dominates and the cratering efficiency
 193 is then dependent not only on velocity, but impactor size. The expression for transient crater
 194 volume is (Holsapple, 1993; Richardson et al., 2007; Dundas et al., 2010):

$$V = K_1 \left(\frac{m_f}{\rho_t} \right) \left(\pi_2 \left(\frac{\rho_m}{\rho_t} \right)^{\frac{1}{3}} + \pi_3^{\frac{2+\mu}{2}} \right)^{-\frac{3\mu}{2+\mu}} \quad (5)$$

195 where K_1 , like μ and \bar{Y} , are experimentally derived properties of the target material. Taking the
 196 transient crater volume to be $(1/24)\pi D_t^3$, assuming the transient crater depth is roughly 1/3 its
 197 diameter, D_t (Melosh 1989; Schmidt and Housen, 1987), this equation can be expressed in terms
 198 of final crater diameter

$$D = 1.3K'D \left(\frac{\rho_m}{\rho_t} \right)^{\frac{1}{3}} \left(\pi_2 \left(\frac{\rho_m}{\rho_t} \right)^{\frac{1}{3}} + \pi_3^{\frac{2+\mu}{2}} \right)^{-\frac{\mu}{2+\mu}} \quad (6)$$

199 where $K' = (4K_1)^{1/3}$ for a spherical meteoroid and the factor 1.3 is the ratio of the final rim-to-rim
 200 diameter and the transient crater diameter (Holsapple, 1993). We adopt values for Mars
 201 consistent with dry desert alluvium of $\bar{Y} = 65$ kPa, $\mu = 0.41$, $K_1 = 0.24$, and $\rho_t = 2000$ kg m⁻³
 202 (Holsapple, 1993; Holsapple and Housen, 2007)

203 A minimum impact velocity threshold of 0.5 km s⁻¹ is selected for the formation of
 204 explosive impact crater formation as projectiles with lower speeds are unlikely to generate a
 205 shock wave of sufficient magnitude to crush the target material and excavate an explosive crater
 206 (Popova et al. 2003). The definition of this velocity is not sharply defined and will depend on
 207 target material properties. Pressure wave velocities in competent basalt are typically ~4.5 – 6.5

208 km s⁻¹, with values an order-of-magnitude lower for loose, unconsolidated soils. Apollo seismic
209 investigations found velocities to be ~0.1 – 0.3 km s⁻¹ in the upper 100 m of the lunar regolith
210 (Kovach and Watkins, 1973; Watkins and Kovach, 1973).

211 The initial altitude of the modeled projectiles is 100 km. The gas density at this altitude is
212 reduced by four orders-of-magnitude relative to the atmospheric density at the planet's surface,
213 and thus deceleration (Eq. 1) is reduced by four orders-of-magnitude relative to when the
214 meteoroid is near the surface and is therefore initially negligible. This altitude also represents the
215 approximate transition between the free molecular flow regime and the continuum regime (i.e.
216 Knudsen number ~ 0.1, depending on the object size, for a mean free path of ~ 1 cm).

217 **2.3 Aerodynamic breakup**

218 The fragmentation of meteoroids during their flight through the atmosphere likely influence the
219 resulting SFD of smaller diameter craters, as more than half (56%) of the >200 fresh craters
220 observed by HiRISE are comprised of clusters of individual craters (Daubar et al., 2013).
221 Numerous additional examples of crater clusters have been observed on the surface of Mars
222 (Popova et al., 2007) implying that the fragmentation of meteoroids that penetrate deep into the
223 atmosphere is a common phenomenon on Mars. The aerodynamic breakup of a projectile is
224 expected when the dynamic pressure experienced during entry, $\rho_a v^2$, exceeds the bulk strength,
225 σ_m , of the projectile. Boulders entering the terrestrial atmosphere display a wide range of strengths
226 inferred from the broad range of observed breakup event altitudes with bulk strengths shown to
227 be ~0.1 – 10 MPa (Ceplecha et al., 1998; Popova et al., 2011). The estimated bulk strengths are
228 low compared to the tensile strength of recovered samples (typically 1-10 %), implying fractures
229 and other zones of weakness within the bodies determine bulk strength rather than material
230 composition (Popova et al., 2011). Dynamic pressures experienced by projectiles entering the

231 Martian atmosphere will commonly exceed 1 MPa and therefore fragmentation should be
232 expected, albeit at a lower altitude than observed in the terrestrial atmosphere.

233 Larger, faster objects experience greater dynamic pressure during flight (Figure 4).
234 Though there is no explicit size dependence on dynamic pressure, smaller objects begin to ablate
235 and decelerate higher in the atmosphere, and therefore experience smaller peak loading at higher
236 altitudes than equivalent larger objects. This implies a size dependence on fragmentation from
237 entry dynamics alone. Further, it is anticipated that larger objects are inherently weaker as they
238 likely contain a greater number of defects, and a power law relation based on statistical strength
239 theory (Weibull, 1951) between bulk strength and sample mass is typically assumed in models
240 (e.g. Artmieva and Shuvalov, 2001; Popova et al., 2003; Svetsov et al., 1995). However, recent
241 analysis of meteorite fall observations in the terrestrial atmosphere suggests that, at least for
242 stony objects, the relation between bulk strength and sample mass may be weaker (Popova et al.,
243 2011). A possible size dependence on fragmentation was reported by Ivanov et al. (2010) based
244 on a preliminary analysis of ~70 fresh craters, and is also exhibited by the 44 fresh craters
245 observed by Daubar et al. (2013), 25 of which consist of two or more craters (57%). This
246 percentage increases for craters with $D > 5$ m to 73% and decreases to 41% for craters with $D <$
247 5 m.

248 **3. Results**

249 **3.1 Fragmentation**

250 The effects of fragmentation on the crater SFD is explored with the model. We include
251 aerodynamic break up of meteoroids in the simulation allowing fragmentation to occur when the
252 dynamic pressure exceeds a threshold bulk strength, $\sigma_m = \rho_a v^2$ (Figure 5). Fragmentation is
253 assumed to occur as a single event; however, multiple fragmentation events at different points in

254 a meteoroid's trajectory are sometimes observed during the flight of terrestrial fireballs.
255 Catastrophic fragmentation (a point source type explosion with thousands of fragments) also
256 occurs occasionally. We constrain the number of fragments to 2-100 and each fragment is
257 followed individually to the termination of its flight in order to assess how fragmentation alters
258 the resulting SFD. The number of fragments generated is assumed to follow a power-law
259 probability: we adopt a power-law slope of -1.5 for our nominal model and adjust this value to
260 explore the sensitivity of our results on this exponent. Decreasing the power-law slope results in
261 a more uniform distribution of fragment numbers, while increasing the slope produces a
262 distribution favoring fewer, larger, fragments. A cascade of fragment sizes is then generated by
263 iteratively subtracting random mass fractions from the initial mass which typically results in a
264 small number of larger fragments and many smaller fragments. We additionally explore selecting
265 mass fractions with a uniform random distribution of fragment sizes.

266 The model is run with 10^6 initial projectiles with a minimum allowable projectile
267 diameter of 2 cm. A significant number of these events do not survive, but this minimum value
268 was found to resolve the atmospheric downturn in the resulting crater SFD allowing the smallest
269 permissible craters to form. The same bulk strength is selected for all the projectiles, and
270 adjusted until the ratio of crater clusters to total impacts for $D > 5$ m is similar to the 73%
271 observed for the 44 craters reported by Duabar et al. (2013). We find that a bulk of strength of σ_m
272 = 0.65 MPa best reproduces the observations, as shown in Figure 6, which plots histograms in
273 $\sqrt{2}$ bins of the resulting crater diameters. Both the observed and model craters are dominated by
274 crater clusters at $D > 5$ m of approximately the same fraction. Effective diameters are estimated
275 for the clusters by $D_{eff} = (\sum_i D_i^3)^{1/3}$, which represents the diameter of an equivalent crater due to a
276 non-fragmented meteoroid (Malin et al., 2006; Ivanov et al., 2008).

277 There is a downturn in the SFD of the craters observed by Daubar et al. (2013) at $D \sim 4\text{-}5$
278 m. However, the model craters continue to increase in number at smaller diameter bins down to
279 the $D = 0.24$ m bin in Figure 6. The majority of craters have small diameters < 1 m, and the
280 fraction of clusters in each bin becomes negligible, with the total fraction of all clusters
281 comprising only 4% of the total model crater population. This implies that the atmospheric
282 downturn has not been observed in the fresh craters, and that a significant number of craters with
283 $D < 4\text{-}5$ m have not been identified. The discovery of fresh craters relies on the detection of dark
284 spots in CTX images in dusty regions. A swarm of fragments will disturb a larger surface area
285 creating, in general, larger dark spots. The predominance of single craters at $D < 5$ m indicates
286 that detection will be more challenging as dark spots become inherently smaller relative to D at
287 these sizes, partly explaining the downturn in the observed SFD at 4-5 m.

288 One might conclude that fragmentation, being only 4% of the events, may not be an
289 important process in shaping the SFD. However, crater clusters begin to dominate the SFD at the
290 very diameters that can be reliably detected by CTX, and therefore the effects on absolute ages
291 derived from crater production functions are considered. Comparing the SFD of the model
292 craters with craters produced by the same projectiles with fragmentation suppressed (Figure 7), a
293 difference in age of 7% is obtained when fitting the Hartmann (2005) production function for D
294 > 4 m. The influence of fragmentation on the crater SFD can be increased by taking the
295 probability of the number of fragments generated when σ_m is exceeded as random and uniform,
296 instead of following the -1.5 slope power law (Figure 5b), and a uniform distribution of fragment
297 masses. In this case we obtain a factor ~ 0.69 difference in age relative to the age derived if no
298 fragmentation is allowed to occur (Figure 7b). This represents the case we have considered to
299 have the largest likely influence on the SFD.

300 The change in the crater SFD with fragmentation can be attributed to the mass
301 dependence on ablation and deceleration and corresponding changes in crater scaling, which is
302 not accounted for when calculating effective crater diameters, D_{eff} . Individual fragments
303 experience greater deceleration and ablation per unit volume than the larger parent meteoroid. If
304 enough of the total mass is shifted into a high deceleration/ablation regime when the parent
305 object is broken into individual fragments, D_{eff} may no longer be representative of the crater
306 generated by an equivalent unfragmented meteoroid. If the ratio of D_{eff} to the actual D resulting
307 from the unfragmented projectile is $\ll 1$, then D_{eff} is a poor representation of the equivalent
308 unfragmented crater. In general, $D_{eff}/D < 1$ when $D_{eff} \lesssim 10$ m for the nominal fragmentation
309 case, with the potential reliability of D_{eff} decreasing with size (Figure 8). Scatter in D_{eff}/D values
310 is largely due to variations in meteoroid velocities with lower D_{eff}/D for faster objects. Some
311 events result in D_{eff}/D values slightly greater than 1, predominately at $D_{eff} \gtrsim 10$ m, due to the
312 dependence of impactor size on gravity scaling where crater efficiency decreases with increasing
313 impactor size. Consequently, the crater efficiency can be larger for the fragments than for the
314 parent projectile in some cases.

315 **3.2 Impact-crater isochrons**

316 The technique of dating the Martian surface using predicted crater SFDs for well-preserved
317 surfaces using impact-crater isochrons has been developed over several decades going back to
318 the early lunar exploration of the 1960s (e.g. Hartmann, 1966; Neukum and Wise, 1976;
319 Hartmann, 1999; Neukum and Ivanov, 1994; Hartmann and Neukum, 2001; Hartmann, 2005).
320 Radiometric and exposure ages from Apollo and Luna samples, correlated with crater
321 populations, have anchored the lunar cratering chronology. Scaling lunar isochrons for Mars to
322 account for the ratio of meteoroids at the top of the martian atmosphere relative to the Moon and

323 the difference in gravity and average impact velocity provides a means of understanding the
324 absolute timescale of major geological and geophysical processes on Mars with order of
325 magnitude accuracy. Degradation of craters over time will result in a departure in the crater
326 population from the isochrons. An inflection at $D \sim 1.5$ km separates the isochrons into two
327 branches with different power-law exponents. This inflection, initially observed in the lunar
328 craters, divides the crater distribution into a shallow branch with a slope of ~ 2 and a steep branch
329 of ~ 3 on a log-differential plot. In his latest iteration of Mars isochrons, Hartmann (2005)
330 included an atmospheric model (Popova et al., 2003) to encapsulate the effects of atmospheric
331 entry of meteors resulting in curvature in the isochrons at sub-km crater diameters.

332 During impact, ejecta traveling large distances from a crater are capable of generating
333 isolated secondary craters that could potentially be mistaken for primary craters. What fraction of
334 observed crater populations are primary versus secondary, and the consequence of unidentified
335 secondary craters in dating surfaces, is a matter of debate. McEwen et al. (2005), and McEwen
336 and Bierhaus (2006), argue that small crater populations are dominated by secondary craters,
337 rendering smaller craters unreliable for dating. Hartmann (2005, 2007) however points out that
338 in formulating isochrons, no attempt is made to exclude all secondaries and contends that the
339 accumulation of secondary craters are not “contamination” but rather part of the signal. A
340 population of primary plus secondary craters will have a steeper SFD power law slope than a
341 population devoid of secondary craters, and McEwen et al. (2005) has proposed that the increase
342 in slope of the steep branch of crater SFDs is the result of secondaries.

343 Our approach of using the observed projectile production function at the top of the
344 terrestrial atmosphere provides an opportunity to independently test the veracity of lunar and
345 martian isochrons. We can also constrain the potential influence of secondary craters, as our

346 Monte Carlo model only produces primary crater populations. If secondary craters are a
347 substantial fraction of crater populations, then our model crater SFD should deviate in both slope
348 and age from the isochrons. Additionally, since we use the present-day flux of projectiles, any
349 significant deviation in age estimates can be attributed to a variation in impact rate over time.

350 We test our model against crater counts conducted on the proximal ejecta of the crater
351 Zunil. The crater Zunil is selected because it is likely the last $D = 10$ km scale crater to form on
352 Mars (McEwen et al., 2005; Hartmann et al., 2010) with an estimated age of ~ 1 Ma based on the
353 isochrons of Hartmann (2005), so the distribution of small craters on its ejecta are likely to be
354 predominately primary. Crater counts were conducted on a ~ 5 km² area north of the crater rim
355 (Figure 9). The resulting crater SFD is consistent with an age ~ 1 Ma, similar to counts conducted
356 by Hartmann et al. (2010). We then modeled a population of craters over a 1 Myr period of time
357 for the same surface area as our crater counts. The resulting SFD from both the counts and the
358 Monte Carlo model overlap for bins $D > 2$ m and fall near the 1 Myr isochron of Hartmann
359 (2005) with a similar slope on a log-differential plot (Figure 9b). Cumulative crater frequencies
360 are also shown (Figure 9c), and yield effective crater retention ages of 0.903 ± 0.077 Ma and
361 0.820 ± 0.071 Ma for the counts and the model respectively. Effective diameters from the crater
362 counts were determined by assuming any craters within 40 m of each other were part of a cluster.
363 For comparison, the SFD of the individual observed craters and model craters result in a modest
364 upward revision of ages to $1.03^{+0.078}_{-0.077}$ Ma and 0.966 ± 0.074 Ma respectively (Figure 9d). As
365 crater densities increase on a surface, the identification of individual clusters becomes more
366 difficult, making age determinations more challenging for smaller craters on older surfaces.

367 We also conducted a similar Monte Carlo comparison with the 44 fresh CTX-CTX
368 detected craters. A crater population is modeled for a corresponding area and time represented by

369 the CTX craters. The model results in a SFD overlapping with the 1 yr isochron of Hartmann
370 (2005). However, the fresh craters fall below the isochron as noted by Daubar et al. (2013). The
371 largest crater, $D = 33.8$ m, is consistent with a single $D \sim 30$ m crater predicted to form annually
372 for the scaled observation area. However, smaller diameter bins are inexplicably under-populated
373 (Figures 9,10) Note that the atmospheric downturn is expected to occur at much smaller
374 diameters (sub-meter), and fragmentation will not substantially deplete the SFD at these smaller
375 sizes (Figure 6b). A lack of a contribution from secondaries to the isochrons also cannot explain
376 the discrepancy, as our model predicts a primary SFD with a similar slope and age as the
377 isochron.

378 Fresh craters discovered using MOC by Malin et al. (2006) also have an apparent deficit
379 of craters at all bin diameters when scaled to the 1-yr isochron of Hartmann (2005). The
380 cumulative distribution of fresh craters, including both CTX-CTX and MOC detections, is shown
381 in Figure 10. The MOC SFD has been scaled to an equivalent time/area for comparison. The
382 MOC camera, with a lower resolution, did not detect any craters below $D \sim 10$ m and detected
383 fewer craters in all bin sizes that overlap with the CTX craters. All bin sizes (except for the
384 largest CTX crater) fall below the isochron, and this discrepancy is greater in the lower
385 resolution dataset. This indicates that observational bias may be the best explanation for the
386 difference between the predicted SFD and the observed SFDs. If this is the case, then over time,
387 as additional, larger diameter craters are identified by CTX/HiRISE, the SFD will start to overlap
388 with the isochron at larger diameter bins since the larger craters are more likely to create
389 detectable dark spots on the surface. This would then suggest that fresh craters were
390 undercounted by MOC at all diameters observed.

391 **3.3 Lunar crater counts**

392 As an additional test, we compare results from the model with crater counts of small craters on
393 the moon (Figure 11). The ejecta of North Ray crater was selected for its relatively young age,
394 which has been constrained by cosmic ray exposure ages of Apollo 16 samples to be ~50 Ma
395 (Arvidson et al., 1975). Our small (0.1 km²) study area only contains craters $D \leq 22$ m. Applying
396 the cratering chronology of Neukum et al. (2001), an age of 58.9 ± 11 Ma is derived from the
397 resulting cumulative SFD, consistent with the age derived by Hiesinger et al., (2012) using a
398 larger overlapping area.

399 A population of projectiles is then generated, again using the size distribution of small
400 near-Earth objects colliding with the terrestrial atmosphere (Brown et al., 2002) and the velocity
401 distribution of Marchi et al. (2009), for a period of 58.9 Ma. This results in a total of 42895
402 craters for the 0.1 km² surface area using projectiles >0.02 m diameter. Crater scaling parameters
403 appropriate for the lunar regolith are employed assuming a regolith strength of 10 kPa, $K_I =$
404 0.132, and $\rho_t = 1500$ kg m⁻³ (Holsapple, 1983; Holsapple and Housen, 2007; Vasavada et al.,
405 2012). The resulting SFD of the Monte Carlo model craters results in a similar age of 57.2 ± 11
406 Ma (Figure 11). This demonstrates the usefulness of our approach, as we are able to reproduce a
407 ~50 – 60 Ma surface age on the Moon using a limited area containing only small craters. If
408 craters in this area were predominately secondary craters at these diameters, then our Monte
409 Carlo model should have predicted a much younger surface age. A similar approach was taken
410 by Ivanov (2006) to demonstrate that small craters on the Moon must be predominately primaries
411 on young surfaces (≤ 100 Ma), consistent with our model.

412 Our ability to reproduce isochron ages using a small area with a limited range of
413 diameters not only validates the applicability of small craters for dating young < 60 Ma surfaces,
414 but also indicates that the cratering rate has on average been constant over this period (Ivanov,

415 2006). How secondary craters alter the SFD and whether such small craters can be reliably used
416 for age dating surfaces in all cases is beyond the scope of this work, but our Monte Carlo
417 approach does independently confirm that crater-count chronometry systems can accurately date
418 the youngest surfaces on both the Moon and Mars.

419 **3.4 Sensitivity analysis**

420 The sensitivity of our results to changes in model parameters is evaluated (Table 2). Our nominal
421 case results in a good fit to the Hartmann (2005) annual isochron for $D \geq 20$ m where the model
422 produces a SFD that results in an age of 1.03 ± 0.017 yr (Figure 12). The Monte Carlo model
423 does not produce as close a match at smaller sizes where the SFD is best fit with an age of 0.734
424 ± 0.0018 yr for $D = 4 - 20$ m. This may result from a greater atmospheric influence on the
425 meteoroids at smaller sizes than predicted by the atmospheric model of Popova et al. (2003) that
426 is incorporated into the isochron, or could be due to Hartmann (2005) assuming gravity scaling
427 only which would also result in less downturn in the isochron as crater scaling transitions into the
428 strength regime (Williams et al. 2010).

429 The mass of the atmospheric column that a meteoroid must traverse will depend on the
430 location of the event as the elevation of the surface can vary substantially. The highest elevation,
431 the summit of Olympus Mons, is ~ 21 km above datum, while at the other extreme, the interior of
432 Hellas Basin, is ~ 8 km below. This represents a range of over 2.5 atmospheric scale heights. One
433 of the most striking characteristics of the topography is that its distribution is bimodal due to the
434 north-south dichotomy in crust thickness (Smith et al., 1999). The more heavily cratered
435 highlands in the southern hemisphere have an average elevation of ~ 1.5 km while the
436 distribution of lowland elevations narrowly peak ~ 5.5 km lower than the highlands (Aharonson
437 et al., 2001). This translates to an increase in average atmospheric density at the surface by a

438 factor 1.6 between the southern highlands, $\rho_o = 0.0135 \text{ kg m}^{-3}$, and the northern lowlands, $\rho_o =$
439 0.0222 kg m^{-3} . Taking the same model projectiles and generating craters for the two atmosphere
440 densities representative of the average elevations of the highlands and lowlands, two crater SFDs
441 are generated for comparison (Figure 12b). Craters $D \geq 20 \text{ m}$ result in ages 1.14 yr and 0.993 yr
442 respectively, bracketing the nominal model results. This is a change of +10.7% and -3.6%.
443 Fitting the smaller diameters, $D = 4 - 20 \text{ m}$, results in ages 0.92 yr and 0.69 yr, a change of
444 25.3% and -6.0%. The greater sensitivity at the small crater diameters is to be expected as
445 smaller projectiles are more sensitive to atmospheric conditions.

446 Increasing and decreasing the ablation coefficients, σ , has a similar effect as changing the
447 atmospheric surface density, as an increase in the rate of mass loss results in smaller objects
448 which in turn results in greater deceleration. Models for the same projectiles with ablation
449 coefficients half the nominal values and double the nominal values were run (Figure 12c). The
450 derived ages for craters $D \geq 20 \text{ m}$ increased by 13.5% and decreased by 18.2% for $\sigma \times 1/2$ and
451 $\sigma \times 2$ respectively, and similarly for craters $D = 4 - 20 \text{ m}$ increased by 28.9% and decreased by
452 30.4%.

453 The model assumes that the different taxonomic types of fireballs distinguished from the
454 larger Earth-entering meteoroids (Ceplecha et al., 1998; Popova et al., 2003) have the same
455 fractional distribution at Mars. These types of fireballs differ in their ability to penetrate the
456 atmosphere and therefore if the proposed fractions of projectiles are substantially different on
457 average from that observed in the terrestrial atmosphere (Ceplecha et al., 1998), the results will
458 change. For example, a greater percentage of higher density objects will experience less
459 deceleration and result in larger craters for a given population of projectiles. The smallest craters
460 in the simulation, cm-scale, are formed exclusively by iron objects due to their high density

461 (7800 kg m⁻³). Iron meteors however are a small fraction of the total population (3%). The
462 majority of the objects are Ordinary Chondrites (29%), Carbonaceous Chondrites (33%), and
463 Cometary Material (26%). None of the Soft Cometary Material objects, with a density of 270 kg
464 m⁻³, survive passage through the martian atmosphere. To demonstrate the sensitivity of the
465 model results to different projectile compositions, we run the simulation assuming pure
466 compositions of the three predominant types: Ordinary Chondrites, Carbonaceous Chondrites,
467 and Cometary Material (Figure 12d). The Ordinary Chondrites, with a density greater than the
468 average combined density, results in a factor >2 increase in age, while the Carbonaceous
469 Chondrites reduce the age by 37.3% for $D = 4 - 20$ m and 15.3% for $D \geq 20$ m. A meteor
470 population comprised entirely of Cometary Material results in substantially younger age
471 estimates, 0.0466 and 0.15 yr for the small and large diameters respectively, younger than the
472 ages derived from either the MOC or CTX-CTX craters, with a slope that deviates from the
473 isochron increasingly at smaller D . The crater counts from Zunil in Figure 9c are shown in
474 Figure 12d for comparison, scaled to the 1yr isochron, showing a slope consistent with a
475 population of objects with average density similar to the nominal values assumed and
476 inconsistent with a substantial fraction of icy, low-density impactors.

477 The crater scaling becomes increasingly sensitive to the target material properties as
478 projectile diameters decrease with weaker material producing a larger crater for a given
479 projectile. Details of the target properties, particularly the effective strength, may not be well
480 constrained and can vary by location, feature, or geologic unit. Dundas et al. (2010) has
481 demonstrated how this can complicate geologic interpretation as surfaces of the same age, but
482 differing material properties, may yield different ages. We explore the sensitivity of the model to
483 a range of target properties. Figure 12e shows the results for the same population of projectiles

484 for four different targets. We take the lunar regolith of section 3.3 as a lower bound on target
485 strength representing a low density, dry, moderately porous soil, and soft rock and hard rock
486 from Holsapple (1993) for two targets with greater strength and density than our nominal Mars
487 regolith. For the rock materials, $\mu = 0.55$, the higher value reflecting lower porosity and therefore
488 less energy dissipation (Holsapple and Housen, 2007), and $K_1 = 0.20$. The densities are assumed
489 to be 2250 and 2500 kg m⁻³ and the material strengths 7.6 and 18.0 MPa for the soft rock and
490 hard rock respectively (Holsapple, 1993; Richardson et al., 2007). The hard rock gives an upper
491 bound representative of competent, young basalt that lacks a substantial regolith cover.

492 The discrepancy in ages between resulting crater SFDs of the different target materials
493 increases with decreasing D . The populations begin to converge $D \gtrsim 100$ m. For $D > 20$ m, the
494 lunar regolith model yields a similar age to the nominal model however for smaller craters, the
495 weaker target material results in larger craters and a corresponding increase in estimated age,
496 0.903 versus 0.734 yr. The stronger rock materials yield smaller craters and the decrease in
497 estimated ages with the rock materials results in SFDs that overlap with the observed CTX-CTX
498 and MOC fresh craters (Figure 12e). For our model to be consistent with the SFD of the fresh
499 craters, the majority of the craters would have to have formed in relatively strong, competent
500 rock. Many of the craters are on Amazonian units in the Tharsis region which is dominated by
501 Amazonian lava flows, however, the largest CTX crater, $D = 33.8$ m, formed on the southeast
502 flank of Pavonis Mons on a relatively young Amazonian volcanic unit (Scott et al., 1998). This
503 crater is consistent with Hartmann 2005 which predicts an annual $D \sim 30$ m diameter crater and
504 its presence in the fresh crater population cannot be attributed to the crater having formed in
505 weaker target material relative to the other fresh craters. It is tempting to dismiss the single crater
506 as a statistical outlier. However, it is incorrect to interpret the \sqrt{n} error bars in comparison to

507 model isochrons as these error bars indicate the $1-\sigma$ range of likely *observations* not *models*
508 given the actual number seen. If we wait an additional year, we may observe no additional events
509 of this size. However the real flux of events of this size clearly cannot be 0 given that a single
510 event has been observed and so models with exceedingly low formation rates must be formally
511 rejected (Aharonson, 2007).

512 If continued observations of fresh CTX-CTX craters verify that the current observed SFD
513 is indeed an accurate reflection of the present-day impact crater population, then our model
514 demonstrates that it is possible to constrain the fraction of impactor material types and average
515 target material properties for Mars. For example, a population of impactors with average
516 densities similar or higher than that observed for terrestrial fireballs could be ruled out as they
517 are not consistent with the current CTX-CTX observations.

518 **4. Discussion**

519 The fact that the slope of the Hartmann (2005) isochrons are the same as that derived in
520 our study using the present-day annual flux of terrestrial fireballs implies that the isochron
521 system does not incorporate many unrecognized secondary craters. This is quite surprising
522 considering McEwen et al. (2005) identify $\sim 10^7$ secondary craters generated by the Zunil crater
523 forming impact event at distances up to 3500 km away from the primary crater. This implies that
524 small secondaries should be abundant on the Martian surface. We specifically selected young
525 surfaces to conduct counts that likely reflect a primary crater population so it is not surprising
526 that our counts have similar slopes to our model. The isochron system however, is derived from
527 counts conducted on lunar maria with average ages of 3.5 Ga, surfaces that have had ample time
528 to accumulate secondaries. Obvious secondaries were not included in those counts and
529 presumably only unrecognizable distant secondaries were included. It remains unclear how

530 secondaries are influencing the crater statistics as we do not identify a secondary signal. We have
531 not attempted a systematic survey to identify a range of crater diameters and surface ages where
532 secondaries are influencing the crater SFD, which is beyond the scope of this study, and caution
533 in using small craters remains warranted as this remains an unresolved issue. However, we do
534 demonstrate that for young surfaces that are not likely contaminated by secondaries, useful ages
535 can be derived from crater counts using small craters.

536 **5. Conclusions**

537 Taking the size distribution of the observed annual flux of terrestrial fireballs, scaling the number
538 by 2.6 for Mars, the nominal value of Hartmann (2005), and appropriate velocity distributions
539 for Mars and the Moon, we are able to generate crater populations with a remarkably similar
540 SFD to that predicted by the isochrons of Hartmann (2005) for Mars and Neukum et al. (2010)
541 for the Moon. Our Monte Carlo model generates a population of primary craters, implying that
542 the isochrons do not contain a significant secondary crater signal as large numbers of secondaries
543 would result in a steeper isochron slope than predicted by our model. This further implies that
544 the inflection from the shallow branch to the steep branch is not attributable to the addition of
545 unidentified secondary craters. Crater counts conducted on the ejecta blanket of Zunil and North
546 Ray crater yield SFDs with similar slopes and ages as our model— ~1 Ma and ~58 Ma,
547 respectively, for Mars and the Moon—demonstrating that the cratering rate on average has been
548 fairly constant on these bodies over these time periods.

549 We find that the details of the atmospheric model for Mars do not substantially alter the
550 results. The Hartmann (2005) isochrons include an atmospheric model (Popova et al., 2003), and
551 differences between the lowlands and highlands do not result in significant deviations from the
552 Hartmann isochron, nor do variations in assumed ablation coefficients. Fragmentation did not

553 significantly alter the model results and smaller projectiles ($D < 5$ m) typically were decelerated
554 enough to avoid fragmentation. The atmospheric downturn predicted by our model occurs at $D \sim$
555 10-20 cm, corresponding to projectile masses roughly equivalent to the mass of the atmospheric
556 column the objects are traversing. This is well below the downturn observed in the fresh craters
557 detected by CTX at $D = 4$ -5 m (Daubar et al., 2013). The downturn in the CTX SFD is likely due
558 to detection limits of CTX. The largest fresh crater, $D = 33.8$ m, observed, is consistent with our
559 model and the prediction of the Hartmann isochron of one annual $D \sim 30$ m crater; however,
560 fewer craters were observed than predicted by the isochron at smaller diameters. It is possible
561 that $D < 30$ m craters are underrepresented in the observed CTX craters and continued
562 observation, allowing for larger craters to form over a longer observation period, may potentially
563 resolve this question.

564 **Acknowledgements**

565 J.-P. W. and A. P. were supported by a NASA Mars Data Analysis Program Grant Number
566 NNX11AQ64G.

567 **References**

- 568 Aharonson, O. (2007) The modern impact cratering flux at the surface of Mars, *Lunar Planet.*
569 *Sci. Conf.*, 38th, #2288.
- 570 Aharonson, O., M. T. Zuber, and D. H. Rothman (2001) Statistics of Mars' topography from the
571 Mars Orbiter Laser Altimeter' Slopes, correlations, and physical Models, *J. Geophys. Res.*,
572 106, 23,723–23,735.
- 573 Artmieva, N. A., and V. V. Shuvalov (2001) Motion of a fragmented meteoroid through the
574 planetary atmosphere, *J. Geophys. Res.*, 106, 3297–3309.

575 Arvidson, R., G. Crozaz, R. J. Drozd, C. M. Hohenberg, C. J. Morgan (1975) Cosmic ray
576 exposure ages of features and events at the Apollo landing sites, *Moon*, 13, 259–276.

577 Baldwin, B., and Y. Sheaffer (1971) Ablation and breakup of large meteoroids during
578 atmospheric entry, *J. Geophys. Res.*, 76, 4653–4668.

579 Basilevsky, A. T., G. Neukum, S. C. Werner, A. Dumke, S. van Gasselt, T. Kneissl, W.
580 Zuschneid, D. Rommel, L. Wendt, M. Chapman, J. W. Head, and R. Greeley (2009)
581 Episodes of floods in MangalaValles, Mars, from the analysis of HRSC, MOC and THEMIS
582 images, *Planet. Space Sci.*, 57, 917–943.

583 Bland, P. A. and T. B. Smith (2000) Meteorite accumulations on Mars, *Icarus*, 144, 21–26.

584 Bronshten, V. A. (1983) *Physics of meteoric phenomena*, Dordrecht, Reidel. 356 p.

585 Brown, P., R. E. Spalding, D. O. ReVelle, E. Tagliaferri, and S. P. Worden (2002) The flux of
586 small near-Earth objects colliding with the Earth, *Nature*, 420, 294–296.

587 Burr, D. M., J. A. Grier, L. P. Keszthelyi, A. S. McEwen (2002) Repeated aqueous flooding from
588 the Cerberus Fossae: Evidence for very recently extant, deep groundwater on Mars, *Icarus*,
589 159, 53–73.

590 Byrne S., C. M. Dundas, M. R. Kennedy, M. T. Mellon, A. S. McEwen, S. C. Cull, I. J. Daubar,
591 D. E. Shean, K. D. Seelos, S. L. Murchie, B. A. Cantor, R. E. Arvidson, K. S. Edgett, A.
592 Reufer, N. Thomas, T. N. Harrison, L. V. Posiolova, F. P. Seelos (2009) Distribution of
593 Mid-Latitude Ground Ice on Mars from New Impact Craters, *Science*, 25, 1674–1676.

594 Ceplecha, Z., J. Borovička, W. G. Elford, D. O. Revelle, R. L. Hawkes, V. Porubčan, M. Šimek
595 (1998) Meteor Phenomena and Bodies, *Space Sci. Rev.*, 84, 327–471.

596 Chyba, C. F., P. J. Thomas, and K. J. Zahnle (1993), The 1908 Tunguska explosion -
597 Atmospheric disruption of a stony asteroid, *Nature*, 361, 40–44.

598 Daubar, I. J., and A. S. McEwen (2009) Depth to diameter ratios of recent primary impact craters
599 on Mars, *Lunar Planet. Sci. Conf.*, 40th, #2419.

600 Daubar, I. J., S. Byrne, A. S. McEwen, and M. Kennedy (2010) New Martian Impact Events:
601 Effects on Atmospheric Breakup on Statistics, *1st Planetary Cratering Consortium*.

602 Daubar, I. J., A. S. McEwen, S. Byrne, C. M. Dundas, A. L. Keske, G. L. Amaya, M. Kennedy,
603 and M. S. Robinson (2011) New craters on Mars and the Moon, *Lunar Planet. Sci. Conf.*,
604 42nd, #2232.

605 Daubar I. J., A. S. McEwen, S. Byrne, M. R. Kennedy, and B. Ivanov (2013) The current martian
606 cratering rate, *Icarus*, in press

607 Davis, P. M. (1993) Meteoroid impacts as seismic sources on Mars, *Icarus*, 105, 469–478.

608 Dundas, C. M., and S. Byrne (2010) Modeling Sublimation of Ice Exposed by Recent Impacts in
609 the Martian Mid-Latitudes, *Icarus*, 206, 716–728.

610 Dundas C. M., L. P. Keszthelyi, V. J. Bray, and A. S. McEwen (2010) Role of material
611 properties in the cratering record of young platy-ridged lava on Mars, *Geophys. Res. Lett.*,
612 37, L12203, doi:10.1029/2010GL042869.

613 Flynn, G. J., and D. S. McKay (1990) An assessment of the meteoritic contribution to the martian
614 soil, *J. Geophys. Res.*, 95, 14,497–14,509.

615 Hartmann, W. K. (1966), Martian cratering, *Icarus*, 5, 565-576.

616 Hartmann, W. K. (1999), Martian cratering VI: crater count isochrons and evidence for recent
617 volcanism from Mars Global Surveyor, *Meteor, Planet. Sci.*, 34, 167-177.

618 Hartmann, W. K. (2005), Martian cratering 8: Isochron refinement and the chronology of Mars,
619 *Icarus*, 174, 294–320.

620 Hartmann, W. K. (2007), Martian cratering 9: toward resolution of the controversy about small
621 craters, *Icarus*, 186, 274–278.

622 Hartmann, W. K. and D. C. Berman (2000), Elysium Planitia lava flows: crater count chronology
623 and geological implications, *J. Geophys. Res.*, 105, 15,011–15,025.

624 Hartmann, W. K., G. Neukum, (2001) Cratering chronology and evolution of Mars. In: Altwegg, K.,
625 Ehrenfreund, P., Geiss, J., Huebner, W.F. (Eds.), *Composition and Origin of Cometary Materials*,
626 Kluwer Academic, The Netherlands, pp. 165–194.

627 Hartmann, W. K., C. Quantin, S. C. Werner, and O. Popova (2010) Do young martian ray craters
628 have ages consistent with the crater count system?, *Icarus*, 208, 621–635.

629 Hiesinger H., C. H. van der Bogert, J. H. Pasckert, L. Funcke, L. Giacomini, L. R. Ostrach, and
630 M. S. Robinson (2012) How old are young lunar craters?, *J. Geophys. Res.*, 117, E00H10,
631 doi:10.1029/2011JE003935.

632 Holsapple, K. A. (1993), The scaling of impact processes in planetary science, *Ann. Rev. Earth*
633 *Planet. Sci.*, 21, 333–373.

634 Holsapple, K. A. and K. R. Housen (2007) A crater and its ejecta: An interpretation of Deep
635 Impact, *Icarus*, 345–356.

636 Ivanov, B. A. (2006) Earth/Moon impact rate comparison: Searching constraints for lunar
637 secondary/primary cratering proportion, *Icarus*, 183, 504–507.

638 Ivanov, B., H. J. Melosh, A. S. McEwen, and the HiRISE team (2008) Small impact crater
639 clusters in high resolution HiRISE images, *Lunar Planet. Sci. Conf.*, 39th, #1221.

640 Ivanov, B. A., H. J. Melosh, A. S. McEwen, and the HiRISE team (2009) Small impact crater
641 clusters in high resolution HiRISE images – II, *Lunar Planet. Sci. Conf.*, 40th, #1410.

642 Ivanov, B. A., H. J. Melosh, A. S. McEwen, and the HiRISE team (2010) Small impact crater
643 clusters in high resolution HiRISE images – III, *Lunar Planet. Sci. Conf.*, 41th, #2020.

644 Kadish, S. J., J. W. Head, R. L. Parsons, D. R. Marchant, (2008) The Ascræus Mons fan-shaped
645 deposit: Volcano–ice interactions and the climatic implications of cold-based tropical
646 mountain glaciation, *Icarus*, 197, 84–109.

647 Kennedy, M. R., and M. C. Malin (2009) 100 new impact crater sites found on Mars, *AGU Fall*
648 *Meeting*, #P43D-1455

649 Kneissel, T., S. van Gasselt, and G. Neukum (2011) Map-projection-independent crater size-
650 frequency determination in GIS environments–New software tool for ArcGIS, *Planet. Space*
651 *Sci.*, 59, 1243–1254.

652 Kovach, R. L., and J. S. Watkins (1973) The velocity structure of the Lunar crust, *The Moon*, 7,
653 63–75.

654 Lanagan, P. D., A. S. McEwen, L. P. Keszthelyi,, T. Thordarson (2001), Rootless cones on Mars
655 indicating the presence of shallow equatorial ground ice in recent times, *Geophys. Res. Lett.*,
656 28, 2365–2367.

657 Love, S. G., and D. E. Brownlee (1991) Heating and thermal transformation of micrometeoroids
658 entering the Earth’s atmosphere, *Icarus*, 89, 26–43.

659 Malin, M. C., and K. S. Edgett (2000a) Evidence for recent groundwater seepage and surface
660 runoff on Mars, *Science*, 288, 2330–2335.

661 Malin, M. C., and K. S. Edgett (2000b) Sedimentary rocks of early Mars, *Science*, 290, 1927–
662 1937.

663 Malin, M. C., and K. S. Edgett (2001) Mars Global Surveyor Mars Orbiter Camera:
664 Interplanetary cruise through primary mission, *J. Geophys. Res.*, 106, 23,429–23,570.

665 Malin, M. C., G. E. Danielson, A. P. Ingersoll, H. Masursky, J. Veverka, M. A. Ravine, and T.
666 A. Soulanille (1992) Mars orbiter camera, *J. Geophys. Res.*, 97, 7699–7718.

667 Malin, M. C., K. S. Edgett, L. Posiolova, S. McColley, and E. Noe Dobrea (2006) Present impact
668 cratering rate and the contemporary gully activity on Mars: Results of the Mars Global
669 Surveyor extended mission, *Science*, 314, 1573–1557.

670 Malin, M. C., J. F. Bell III, B. A. Cantor, M. A. Caplinger, W. M. Calvin, R. T. Clancy, K. S.
671 Edgett, L. Edwards, R. M. Haberle, P. B. James, S. W. Lee, M. A. Ravine, P. C. Thomas,
672 and M. J. Wolff (2007) Context Camera Investigation on board the Mars Reconnaissance
673 Orbiter, *J. Geophys. Res.*, 112, E05S04, doi:10.1029/2006JE002808.

674 Mangold, N. (2003) Geomorphic analysis of lobate debris aprons on Mars at Mars Orbiter
675 Camera scale: Evidence for ice sublimation initiated by fractures, *J. Geophys. Res.*, 108,
676 10.1029/2002JE001885, pp. GDS 2-1.

677 Marquez, A., Fernandez, C., Anguita, F., Farelo, A., Anguita, J., de la Casa, M.-A. (2004) New
678 evidence for a volcanically, tectonically, and climatically active Mars, *Icarus*, 172, 573–581.

679 Marchi, S., S. Mottola, G. Cremonese, M. Massironi, and E. Martellato (2009) A new
680 chronology for the Moon and Mercury, *Astron. J.*, 137, 4936–4948.

681 McEwen, A. S., and E. B. Bierhaus (2006) The importance of secondary cratering to age
682 constraints on planetary surfaces, *Annu. Rev. Earth Planet. Sci.*, 34, 535–567.

683 McEwen, A. S., B. S. Preblich, E. P. Turtle, N. A. Artemieva, M. P. Golombek, M. Hurst, R. L.
684 Kirk, D. M. Burr, and P. R. Christensen (2005), The rayed crater Zunil and interpretations of
685 small impact craters on Mars, *Icarus*, 176, 351–381, doi:10.1016/j.icarus.2005.02.009.

686 McEwen, A. S., E. M. Eliason, J. W. Bergstrom, N. T. Bridges, C. J. Hansen, W. A. Delamere, J.
687 A. Grant, V. C. Gulick, K. E. Herkenhoff, L. Keszthelyi, R. L. Kirk, M. T. Mellon, S. W.
688 Squyres, N. Thomas, C. M. Weitz (2007a) Mars Reconnaissance Orbiter's High Resolution

689 Imaging Science Experiment (HiRISE), *J. Geophys. Res.*, 112, E05S02,
690 doi:10.1029/2005JE002605.

691 McEwen, A. S., J. A. Grant, L. L. Tornabene, S. Byrne, and K. E. Herkenhoff (2007b) HiRISE
692 observations of small impact craters on Mars, *Lunar Planet. Sci. Conf.*, 38th, #2009.

693 McEwen, A. S., L. L. Tornabene, and the HiRISE Team (2007c) Modern Mars: HiRISE
694 observations of small, recent impact craters on Mars, 7th *Int. Conf. Mars*, LPI Contribution
695 No. 1353, #3086.

696 Melosh, H. J. (1989), *Impact Cratering: A Geologic Process*, 245 pp., Oxford Univ. Press, New York.

697 Michael, G. G., and G. Neukum (2009) Planetary surface dating from crater size-frequency
698 distribution measurements: Partial resurfacing events and statistical age uncertainty, *Earth*
699 *Planet. Sci. Lett.*, 294, 223–229.

700 Neukum, G. and D. Wise, (1976) Mars: a standard crater curve and possible new time scale, *Science*,
701 194, 1381–1387.

702 Neukum, G., and B. A. Ivanov (1994), Crater Size Distributions and Impact Probabilities on Earth from
703 Lunar, Terrestrial-planet, and Asteroid Cratering Data, in *Hazards Due to Comets and Asteroids*,
704 edited by T. Gehrels, M. S. Matthews, and A. M. Schumann, pp. 359–416.

705 Neukum, G., B. A. Ivanov, and W. K. Hartmann (2001) Cratering records in the inner solar
706 system in relation to the Lunar reference system, *Space Sci. Rev.*, 96, 55–86.

707 Podolak, M., J. B. Pollack, and R. T. Reynolds (1988) Interactions of planetesimals with
708 protoplanetary atmospheres, *Icarus*, 73, 163–179.

709 Popova, O., I. Nemtchinov, and W. K. Hartmann (2003) Bolides in the present and past martian
710 atmosphere and effects on cratering processes, *Meteorit. Planet. Sci.*, 38, 905–925.

711 Popova, O., W. K. Hartmann, I. Nemtchinov, D. C. Richardson, and D. C. Berman (2007),
712 Crater clusters on Mars: shedding light on martian ejecta launch conditions, *Icarus*, 190, 50–
713 73.

714 Popova, O., J. Borovička, W. K. Hartmann, P. Spurný, E. Gnos, I. Nemtchinov, and J. M. Trigo-
715 Rodríguez (2011) Very low strengths of interplanetary meteoroids and small asteroids,
716 *Meteorit. Planet. Sci.*, 46, 1525–1550.

717 Quantin, C., N. Mangold, W. K. Hartmann, and P. Allemand (2007), Possible long-term decline
718 in impact rates 1. Martian geological data, *Icarus*, 186, 1–10.

719 Reiss, D., S. van Gasselt, G. Neukum, and R. Jaumann (2004) Absolute dune ages and
720 implications for the time of formation of gullies in Nirgal Vallis, Mars, *J. Geophys. Res.*
721 109, E06007, doi:10.1029/2004JE002251.

722 Richardson, J. E., H. J. Melosh, C. M. Lisse, and B. Carcich (2007) A ballistic analysis of the
723 Deep Impact ejecta plume: Determining comet Tempel 1's gravity, mass, and density,
724 *Icarus*, 190, 357–390.

725 Schmidt, R. M., and K. R. Housen (1987), Some recent advances in the scaling of impact and
726 explosion cratering , *Int. J. Impact Eng.*, 5, 543–560.

727 Schon, S. C., J. W. Head, and C. I. Fassett (2009) Unique chronostratigraphic marker in
728 depositional fan stratigraphy on Mars: Evidence for ca. 1.25 Ma gully activity and surficial
729 meltwater origin, *Geology*, 37, 207–210.

730 Scott, D. H., J. M. Dohm, and J. R. Zimbelman (1998) Geologic map of Pavonis Mons volcano,
731 Mars, US Geol. Surv. Misc. Invest. Ser. Map I-2561.

732 Shean, D. E., J. W. Head, M. Kreslavsky, G. Neukum and HRSC Co-I Team (2006) When were
733 glaciers present in Tharsis? Constraining age estimates for the Tharis Montes fan-shaped
734 deposits, *Lunar Planet. Sci. Conf.*, 37th, #2092.

735 Smith, D. E., M. T. Zuber, S. C. Solomon, R. J. Phillips, J. W. Head, J. B. Garvin, W. B.
736 Banerdt, D. O. Muhleman, G. H. Pettengill, G. A. Neumann, F. G. Lemoine, J. B. Abshire,
737 O. Aharonson, C. D. Brown, S. A. Hauck, A. B. Ivanov, P. J. McGovern, H. J. Zwally, T. C.
738 Duxbury (1999) The global topography of Mars and implications for surface evolution,
739 *Science*, 284, 1495–1503.

740 Svetsov, V. V., I. V. Nemtchinov, and A. V. Teterov (1995) Disintegration of large meteoroids in
741 Earth's atmosphere: Theoretical models, *Icarus*, 116, 131–153.

742 Vasavada, A. R., J. L. Bandfield, B. T. Greenhagen, P. O. Hayne, M. A. Siegler, J.-P. Williams,
743 and D. A. Paige (2012) Lunar equatorial surface temperatures and regolith properties from
744 the Diviner Lunar Radiometer Experiment, *J. Geophys. Res.*, 117, E00H18,
745 doi:10.1029/2011JE003987.

746 Watkins, J. S. and R. L. Kovach (1973) Seismic investigation of the lunar regolith, *Proc. Fourth*
747 *Lunar Sci. Conf.*, 3, 2561–2574.

748 Weibull, W. A. (1951) A statistical distribution function of wide applicability, *J. Appl. Mech.*,
749 10, 140–147.

750 Wilhelms, D. E. (1987) The geologic history of the Moon, *U.S. Geol. Surv. Prof. Pap.*, 1348, 302
751 pp.

752 Williams, J.-P., O. Aharonson, and A. V. Pathare (2010) The production of small primary craters
753 on Mars, *Lunar Planet. Sci. Conf.*, 41st, #2574.

754

755

756 **Tables**757 **Table 1**

758 Distribution of material types based on fireball network observations (Ceplecha et al., 1998).

Group	% obs.	Density, ρ_m (kg m ⁻³)	Ablation Coef., σ
Irons	3	7800	7.0×10^{-8}
Ordinary Chondrites	29	3700	1.4×10^{-8}
Carbonaceous Chondrites	33	2000	4.2×10^{-8}
Cometary Material	26	750	10.0×10^{-8}
Soft Cometary Material	9	270	21.0×10^{-8}

759

760

761

762 **Table 2**

763 Sensitivity analysis

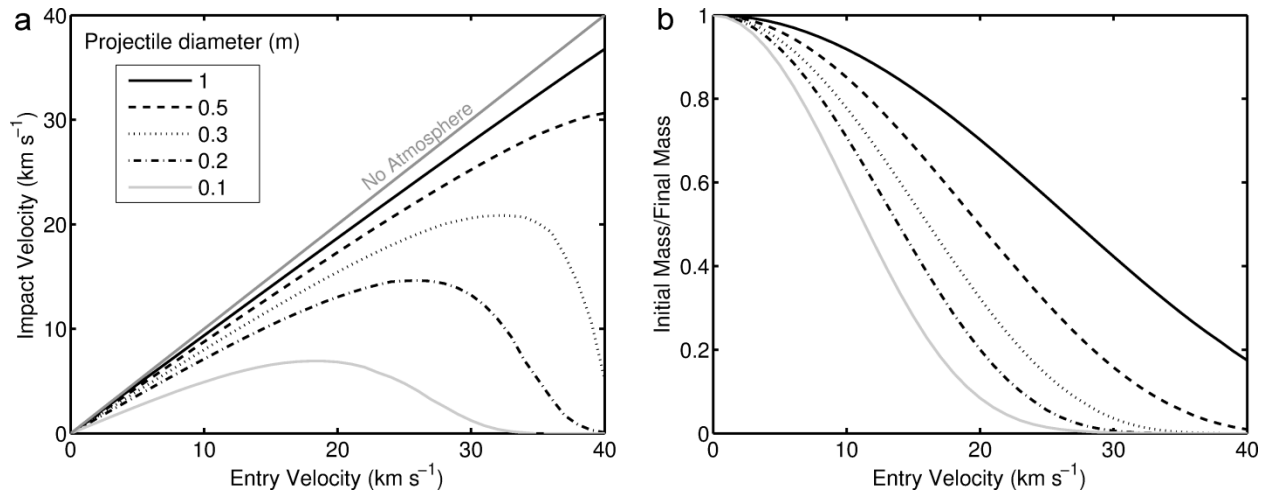
Model (1 yr)	Best-fit ¹ isochron from Hartmann (2005)	
	$D = 4 - 20$ m	$D = 20 - 300$ m
Nominal	0.734 ± 0.002	1.030 ± 0.017
Highlands ($\rho_o = 0.0135$ kg m ⁻³)	0.920 ± 0.002	1.140 ± 0.018
Lowlands ($\rho_o = 0.0222$ kg m ⁻³)	0.687 ± 0.002	0.993 ± 0.017
$\sigma \times \frac{1}{2}$	0.946 ± 0.002	1.170 ± 0.018
$\sigma \times 2$	0.511 ± 0.002	0.843 ± 0.016
Ordinary Chondrite only	1.75 ± 0.003	2.13 ± 0.025
Carbonaceous Chondrite only	0.46 ± 0.002	0.872 ± 0.017
Cometary Material only	0.047 ± 0.001	0.15 ± 0.007
Lunar Regolith	0.903 ± 0.002	0.959 ± 0.016
Soft Rock	0.327 ± 0.001	0.561 ± 0.013
Hard Rock	0.193 ± 0.001	0.295 ± 0.009

¹ Isochrons fit to cumulative SFD using Craterstats2 program (Michael and Neukum, 2009)

764

765

766 **Figures**

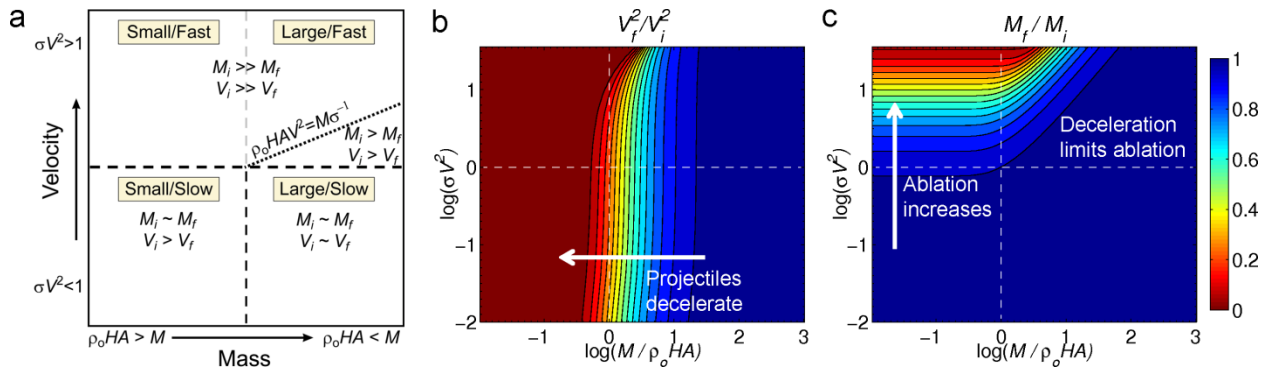


767

768 **Figure 1.** (a) Initial velocity versus final velocity and (b) the ratio of initial and final projectile
 769 mass versus initial velocity for a range of projectile diameters (10 cm – 1 m) where objects have
 770 properties of ordinary chondrites (Table 1). Smaller, faster objects are more effectively
 771 decelerated and ablated.

772

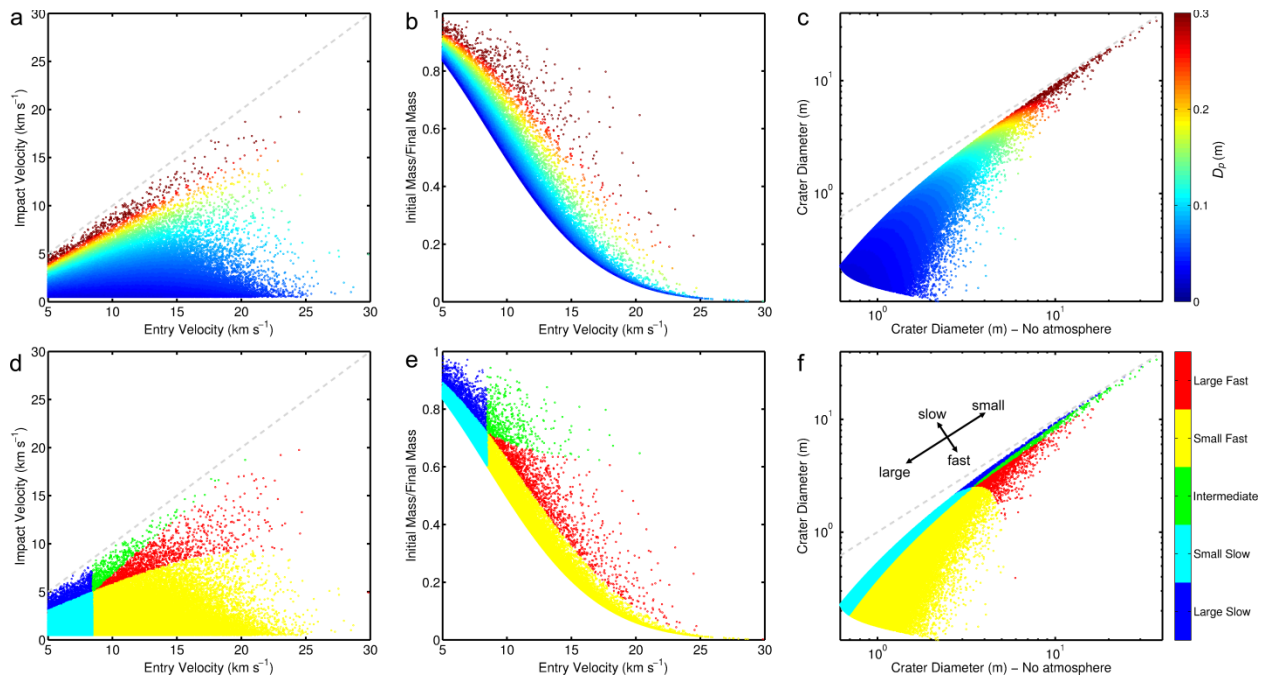
773



774

775 **Figure 2.** (a) General classes of projectiles based on initial mass and velocity. *Large, slow*
 776 *projectiles*: remain relatively unchanged as they are not energetic enough to ablate and too
 777 massive for the atmosphere to decelerate. *Small, slow projectiles*: the mass of the atmospheric
 778 column becomes comparable to the mass of the object and deceleration occurs. *Fast projectiles*:
 779 deceleration and ablation are significant as the energy of traversing a column of atmosphere at a

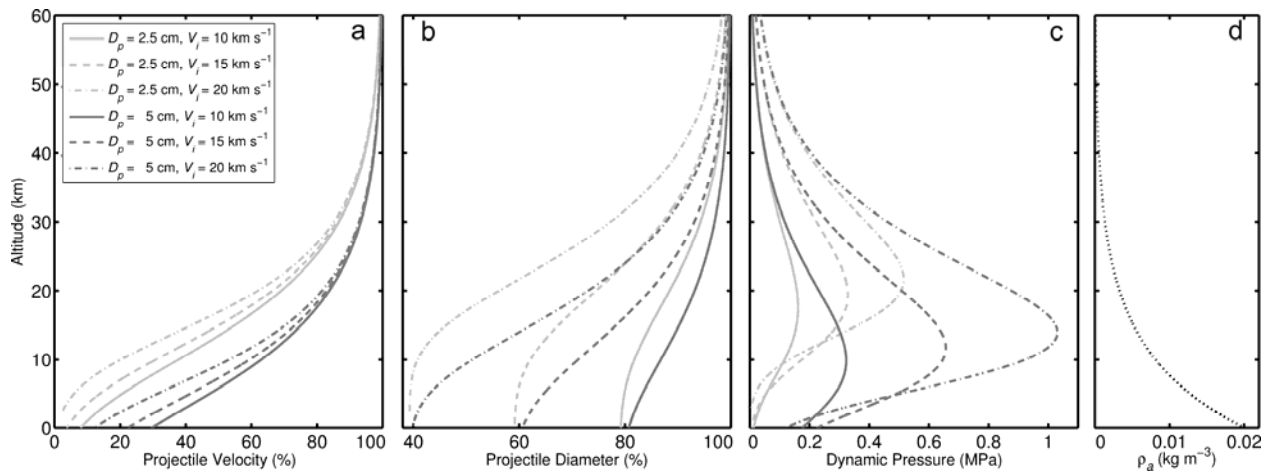
780 given velocity exceeds that required to ablate the entirety of its mass. The triangular wedge
 781 defines intermediate objects that would significantly ablate if deceleration does not occur,
 782 however deceleration limits the ablation. Model results of the ratios of initial and final
 783 (b) velocities and (c) masses are shown for projectile masses non-dimensionalized by the mass of
 784 the atmospheric column encountered on the x-axis and the initial projectile velocity squared by
 785 the energy per unit mass, σ^{-1} , on the y-axis. For $\sigma = 1 \times 10^{-8} \text{ kg J}^{-1}$, slow projectiles have $v_i < 10$
 786 km s^{-1} .
 787



788
 789 **Figure 3.** Scatter plots of results from the Monte Carlo simulation with a bivariate distribution of
 790 velocities and projectile diameters for 2×10^5 events with initial entry angles 45° and ordinary
 791 chondritic compositions. (a) Impact velocity versus initial entry velocity, (b) initial and final
 792 mass ratio versus entry velocity, and (c) final crater diameter versus crater diameter without an
 793 atmosphere, i.e. crater diameter resulting from initial mass and velocity. The color scale of (a-c)
 794 shows the initial projectile diameter. (d-f) are the same as (a-c) but events are tagged with 5

795 colors representing the general class of projectiles as defined in figure 2 (Slow/Fast,
 796 Small/Large). This trend is show with arrows in (f). Deviations from the grey dashed lines in
 797 (a),(c),(d), and (f), and from the horizontal in (b) and (e), shows the magnitude of ablation and/or
 798 deceleration experienced by the objects. Crater diameters are determined assuming parameters of
 799 dry soil with effective strength, $\bar{Y} = 65 \text{ kPa}$ and $\rho_t = 2000 \text{ kg m}^{-3}$ (Holsapple, 1993).

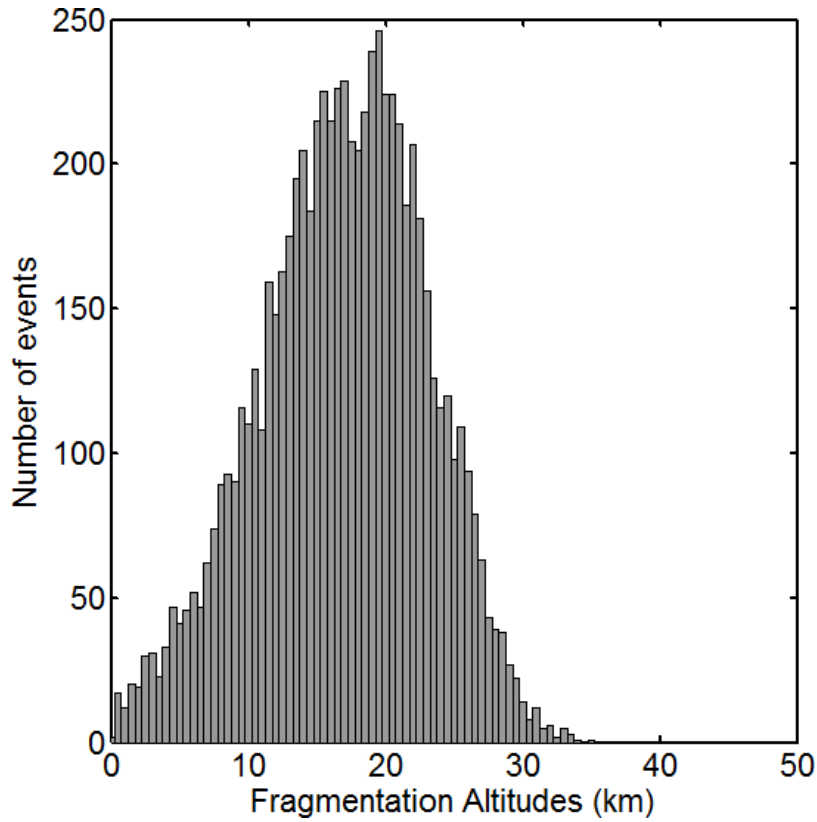
800



801

802 **Figure 4.** Profiles of (a) the percent of initial velocity, (b) the percent of initial diameter, and (c)
 803 the dynamic pressure for six ordinary chondrites in the martian atmosphere as a function of
 804 altitude with entry angles 45° . (d) Assumed atmospheric density with altitude. Note that while
 805 the faster projectiles decelerate to a greater relative extent, they experience larger dynamic
 806 pressure upon entry. Ablation is more sensitive to velocity, however, deceleration is more
 807 sensitive to projectile size, and therefore smaller objects tend to experience lower dynamic
 808 pressures.

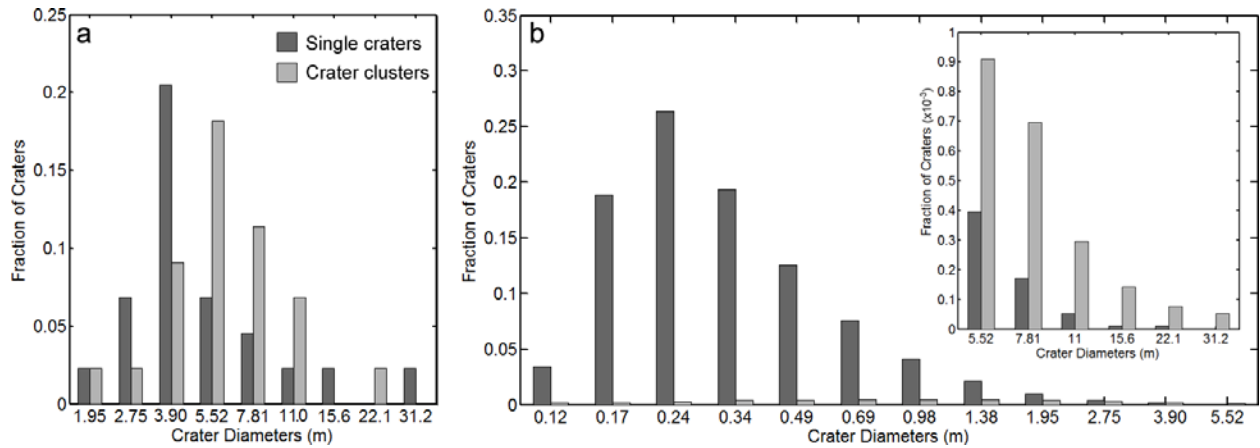
809



810

811 **Figure 5.** Histogram of fragmentation altitudes using $\sigma_m = 0.65$ MPa. Most fragmentation occurs
 812 \sim 2-3 scale heights above the surface with few fragmentation events occurring at lower altitudes.

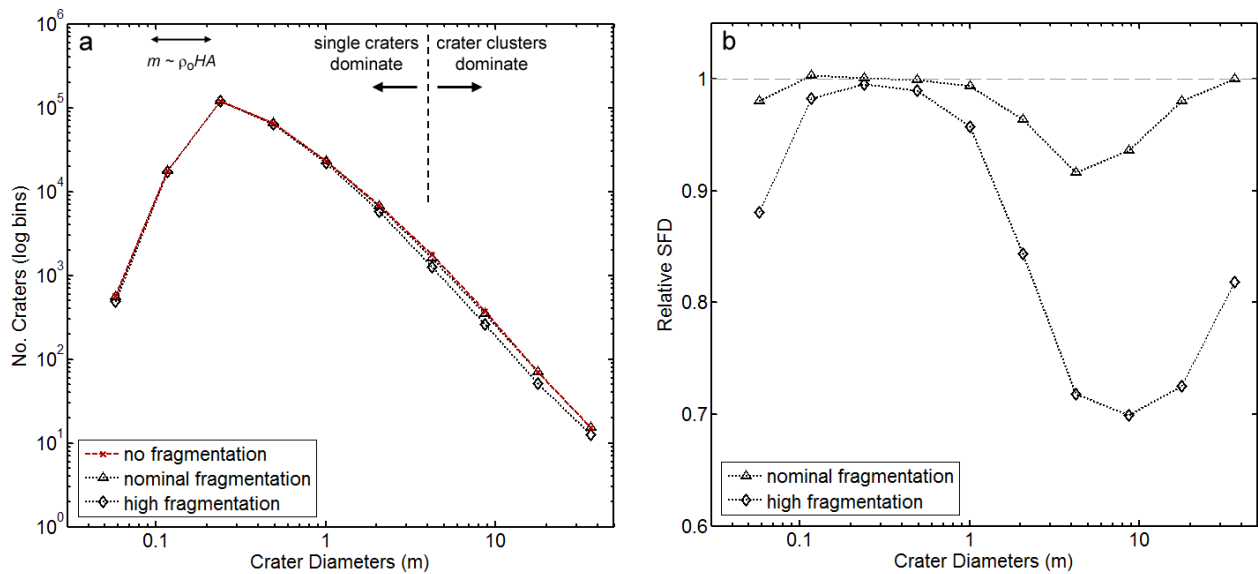
813



814

815 **Figure 6.** Histograms of crater diameters for (a) the 44 fresh craters reported by Daubar et al.
 816 (2013) and (b) the model using $\sigma_m = 0.65$ MPa. Diameters of crater clusters are effective
 817 diameters (see text). The inset is the model craters for $D > 5$ m.

818

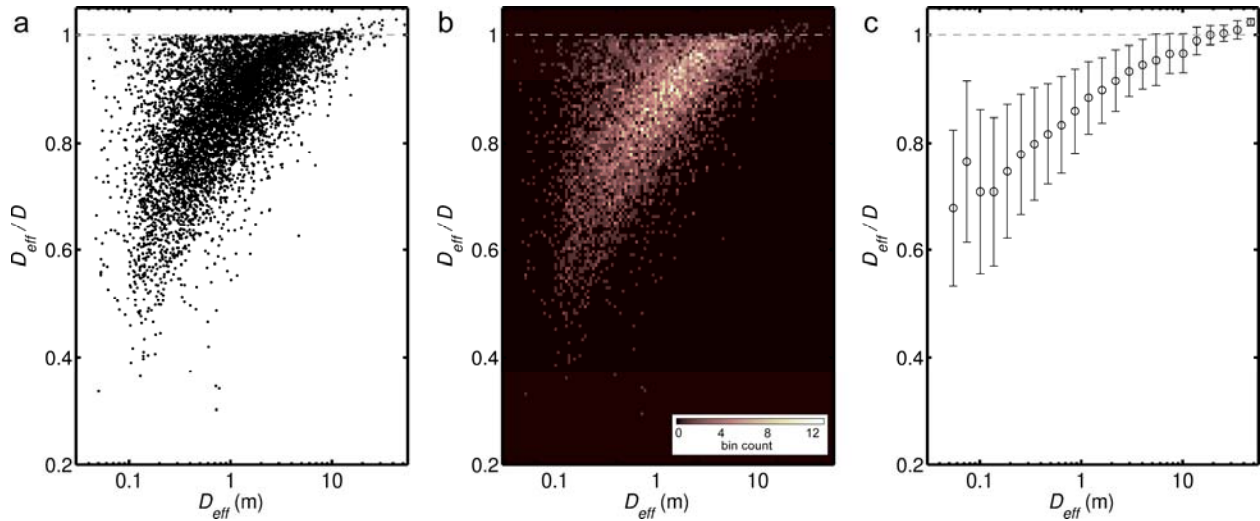


819

820 **Figure 7.** (a) The modeled crater SFDs where no fragmentation occurs (i.e. $\sigma_m \gg \rho_a v^2$ for all
 821 meteoroids) and two different fragmentation characteristics: one favoring fewer fragments with
 822 few large fragments and many small fragments (nominal model), and one with a uniform random
 823 distribution of fragment numbers and sizes to increase the influence of fragmentation on the
 824 crater SFD. (b) The ratio of crater SFDs with and without fragmentation. The influence of
 825 fragmentation on the SFD is greatest at $D \sim 2 - 20$ m.

826

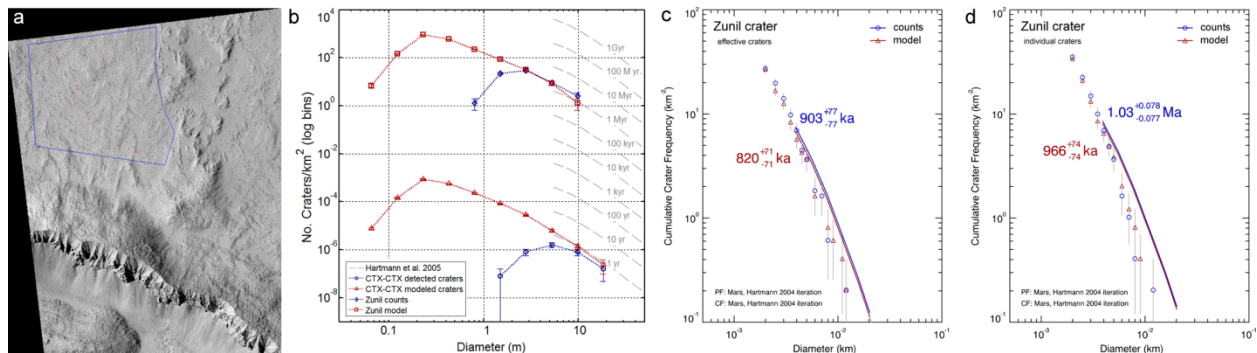
827



828
 829 **Figure 8.** Model D_{eff}/D for: (a) individual crater clusters (b) a 2D histogram and (c) the mean in
 830 log D_{eff} bins. Error bars represent the standard deviation in each bin. D_{eff} is increasingly
 831 unreliable at smaller sizes below ~ 10 m.

832

833

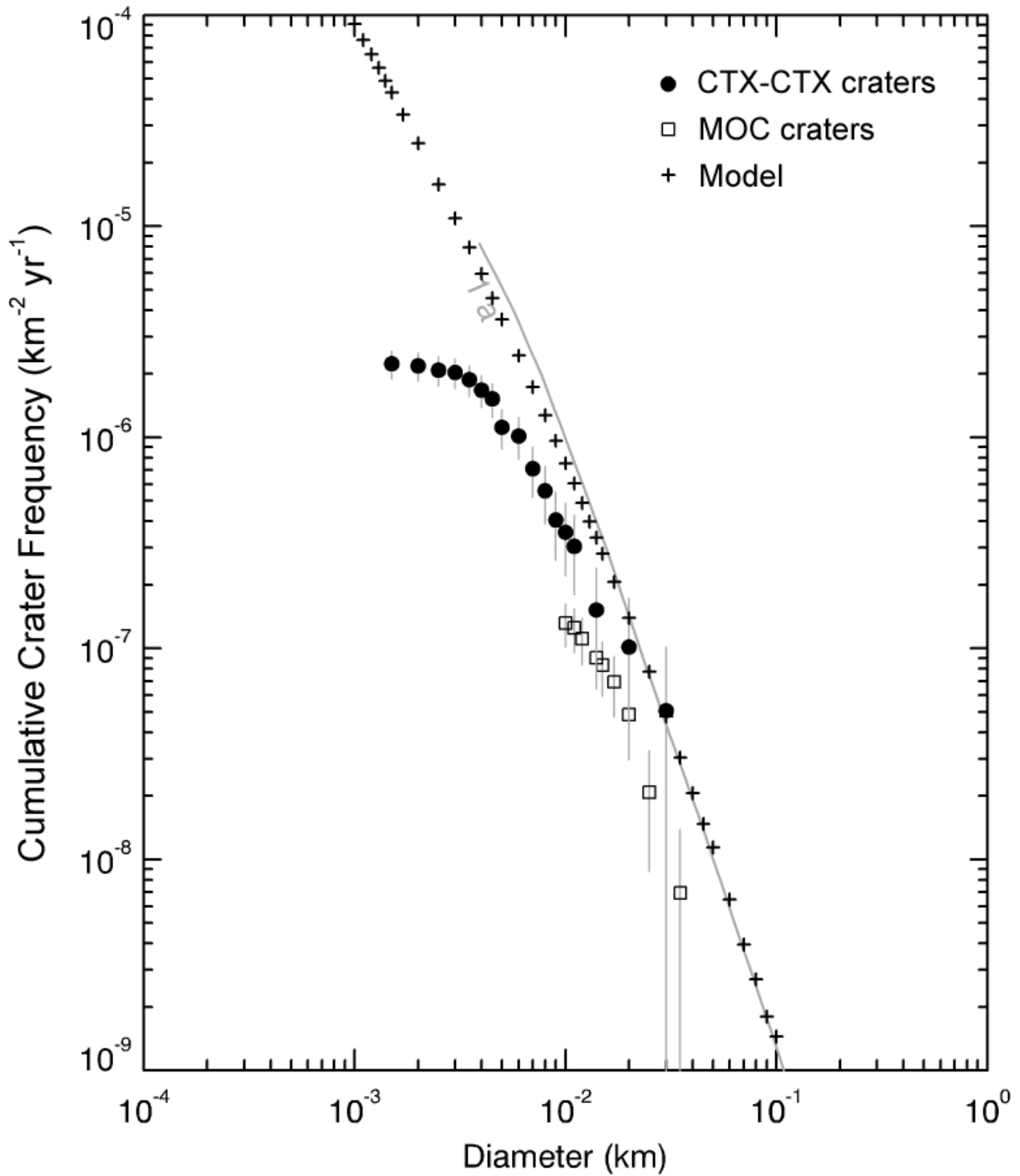


834
 835 **Figure 9.** Crater counts conducted on a ~ 5 km² area north of the Zunil crater rim using HiRISE
 836 image PSP_001764_1880 which was calibrated and map-projected using ISIS (Integrated
 837 Software for Imagers and Spectrometers) and imported into Arcmap, with CraterTools (Kneissl
 838 et al., 2011) used to identify and measure crater diameters. (a) Location of Zunil crater count
 839 area in HiRISE image PSP_001764_1880. (b) Log-differential plot of D_{eff} for crater counts for
 840 Zunil and the 44 new impact sites constrained by CTX (Daubar et al., 2013) (blue) and model

841 results (red) for the corresponding surface area and time. Cumulative crater frequency of (c) D_{eff}
842 and (d) for individual craters for crater counts (blue) and model results (red) using the
843 Craterstats2 software tool (Michael and Neukum, 2009).

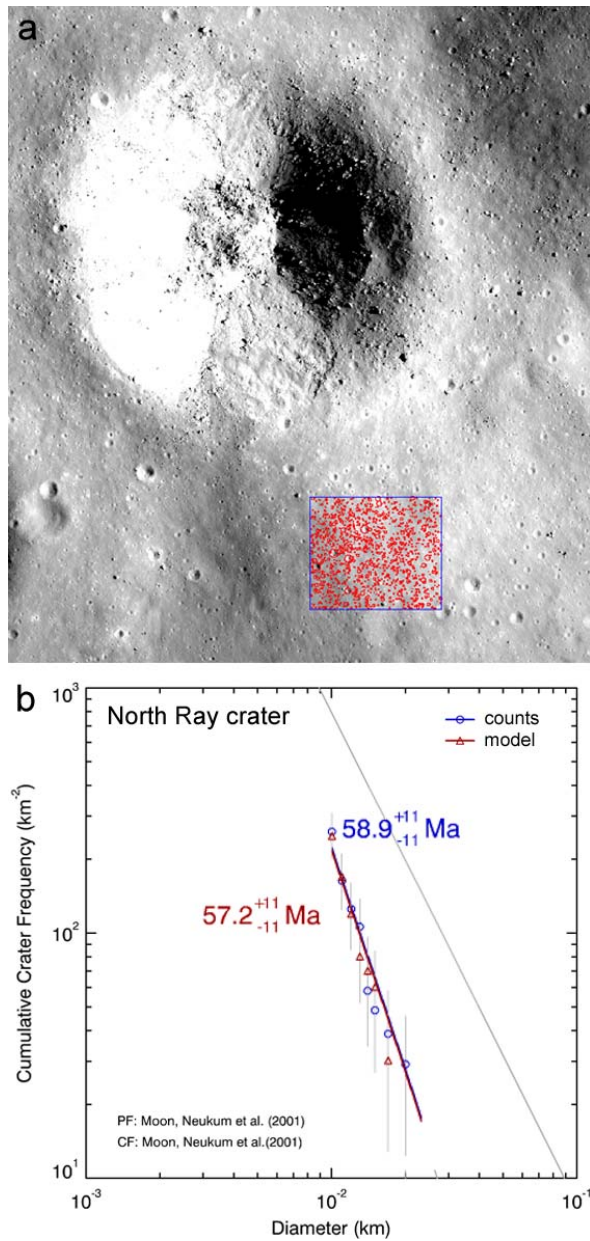
844

845



846

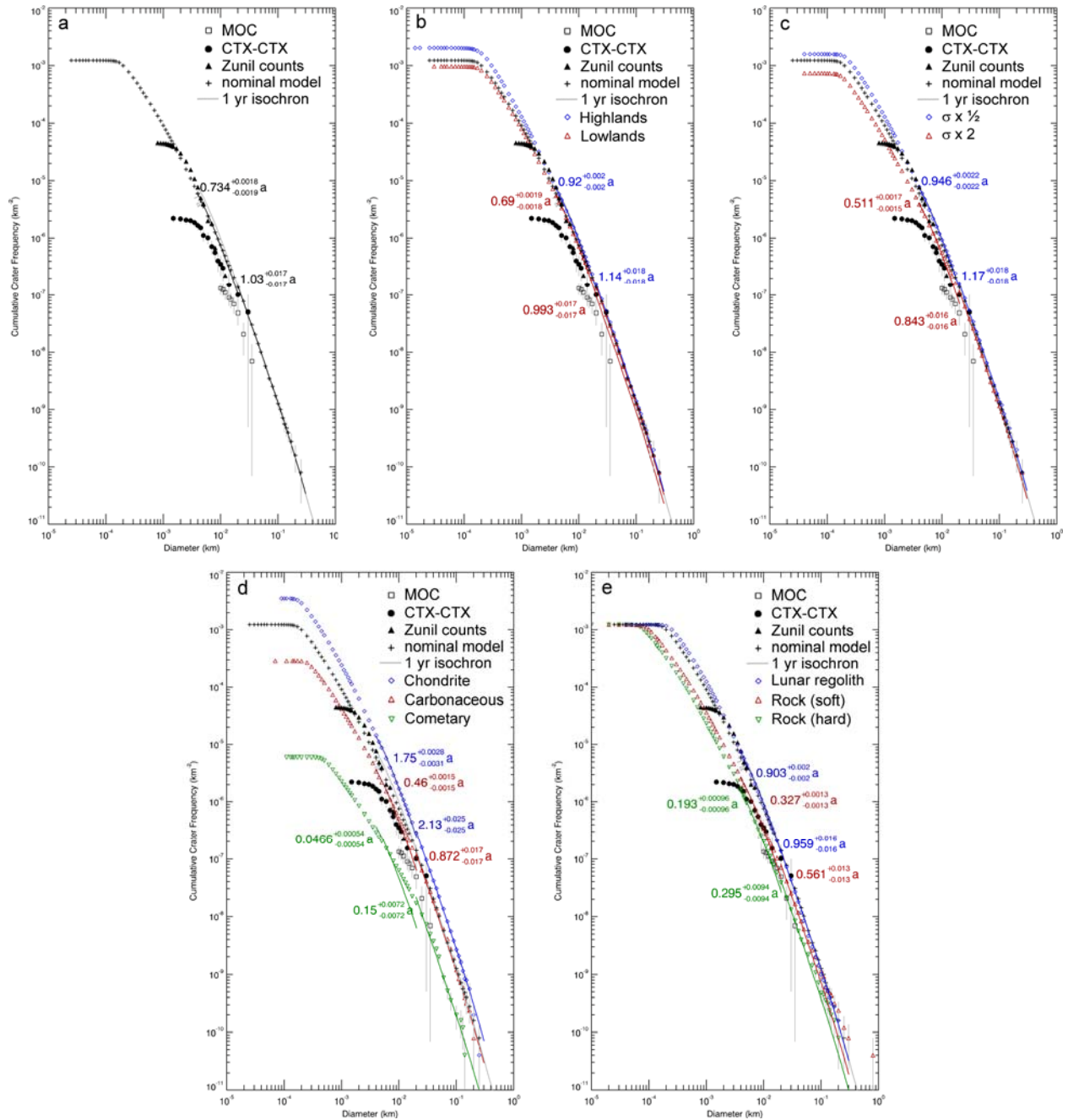
847 **Figure 10.** The cumulative SFD for the fresh craters from CTX-CTX detections (Daubar et al.,
 848 2013), MOC (Malin et al., 2006), and model results, scaled to the same time/area, and the annual
 849 Hartmann (2005) isochron (gray line).



851

852 **Figure 11.** (a) Location of North Ray crater count area (350 m × 300 m blue box) in LRO NAC
 853 image M129187331 (NASA/GSFC/Arizona State Univ.). (b) The cumulative crater frequency of
 854 the crater counts (blue) and the model (red) using the Craterstats2 software tool (Michael and
 855 Neukum, 2009). The gray line indicates crater saturation.

856



857

858 **Figure 12.** Sensitivity of cumulative SFD to model parameters. (a) Nominal model, fresh craters
 859 identified with MOC (Malin et al., 2006), and CTX (Daubar et al., 2013), and counts conducted
 860 on Zunil ejecta scaled to an annual isochron of Hartmann (2005). Estimated ages are for $D = 4 -$
 861 20 m and $D = 20 - 300$ m. Nominal model assumes: $\rho_o = 0.02 \text{ kg m}^{-3}$ consistent with the
 862 elevation of Zunil crater (-2.8 km), the distribution of meteoroid types with corresponding

863 ablation coefficients as given by Ceplecha et al. (1998), and target material properties consistent
864 with dry desert alluvium, $K_1 = 0.24$, $\mu = 0.41$ and $\bar{Y} = 65$ kPa. (b) Results for atmospheric surface
865 densities for the Highlands and Lowlands. (c) Results scaling the ablation coefficients, σ , by 0.5
866 and 2. (d) Results assuming all projectiles made of ordinary chondrites, carbonaceous chondrites,
867 or cometary material as defined in Table 1. (e) Results assuming target material properties of
868 lunar regolith, soft rock, and hard rock.